Journal of Materials Processing Tech. 317 (2023) 117985

Contents lists available at ScienceDirect

Journal of Materials Processing Tech.

journal homepage: www.elsevier.com/locate/jmatprotec

Tailoring absorptivity of highly reflective Ag powders by pulsed-direct current magnetron sputtering for additive manufacturing processes

Matthew D. Wadge [a,*,1], Morgan Lowther [b,c,**,1], Timothy P. Cooper [d], William J. Reynolds [e], Alistair Speidel [d], Luke N. Carter [b], Daisy Rabbitt [b], Zakhar R. Kudrynskyi [a], Reda M. Felfel [a,f,g], Ifty Ahmed [a], Adam T. Clare [d,h], David M. Grant [a], Liam M. Grover [b], Sophie C. Cox [b]

[a] Advanced Materials Research Group, Faculty of Engineering, University of Nottingham, UK
[b] Healthcare Technology Institute, School of Chemical Engineering, University of Birmingham, UK
[c] School of Mechanical and Design Engineering, University of Portsmouth, UK
[d] Advanced Component Engineering Laboratory, Faculty of Engineering, University of Nottingham, Nottingham, UK
[e] Centre for Additive Manufacturing, Faculty of Engineering, University of Nottingham, Nottingham, UK
[f] Physics Department, Faculty of Science, Mansoura University, Mansoura, Egypt
[g] Advanced Composites Group, University of Strathclyde, Glasgow, Scotland, UK
[h] Department of Mechanical Engineering, University of British Columbia, Vancouver, Canada

ARTICLE INFO

Associate Editor: Marion Merklein

Keywords:
Additive manufacturing
Magnetron sputtering
Laser powder bed fusion
Physical vapour deposition

ABSTRACT

Processing of highly reflective and high thermally conductive materials (Cu, Ag, etc.) by laser powder bed fusion (LPBF) is of increasing interest to broaden the range of materials that can be additively manufactured. However, these alloys are challenged by high reflectivity resulting in unmelted particles and porosity. This is exacerbated for in-situ alloying techniques, where divergent optical properties of blended powders further narrow the stable processing window. One possible route to improved uniformity of initial melting is through coating powders with an optically absorptive layer. In-situ alloying of Ti-Ag was chosen as a model to assess this, given the potential of Ti-Ag as a novel antimicrobial biomedical alloy, facilitating an ideal model to assess this approach. High purity Ag powder was coated with Ti via physical vapour deposition. Barriers to reliable coating were investigated, with agglomeration of particles observed at a sputtering power of 100 W. In-situ laser micro calorimetry demonstrated a significant improvement in melting performance for coated Ag powder, with continuous tracks attained at 280 W vs. 320 W for uncoated powder, and absorptivity increasing from 27 % to 45 % at 320 W incident laser power. Subsequent in-situ alloying of the Ag powder when blended with commercially pure Ti powder demonstrated that improved absorptivity allowed for more uniform densification of the blended powder bed at lower energy density (0.7 ± 1.0 vs 7.1 ± 2.0 % porosity at 133 $J.m^{-1}$). Ultimately, this offers a promising route to improved alloy development via LPBF, through application of a homogeneous, relevant coating.

1. Introduction

Metal additive manufacturing (AM) processes have enabled entirely new approaches to alloy development, particularly the use of powder feedstock for laser powder bed fusion (LPBF), direct energy deposition techniques, sintering methods, as well as the production of metal matrix composites (ASTM, 2015). While some materials respond well to LPBF, highly reflective materials and those with very high thermal conductivity, most notably the noble metals (e.g., Ag, Au, Pt etc.), can be severely limited by small process windows making process optimisation difficult, time consuming and expensive. However, these same properties give these alloys wide-ranging high-value applications, such as high performance heatsinks (Sciacca et al., 2022), bespoke bicontinuous electrodes (Pang et al., 2020) and radio frequency wave guides for satellite telecommunications (Seltzman and Wukitch, 2021). Ag and Cu see further application for their antimicrobial properties, with possible

* Corresponding author.
** Corresponding author at: Healthcare Technology Institute, School of Chemical Engineering, University of Birmingham, UK.
E-mail addresses: matthew.wadge3@nottingham.ac.uk (M.D. Wadge), morgan.lowther@port.ac.uk (M. Lowther).
[1] Dr Matthew Wadge and Dr Morgan Lowther are joint first authors

https://doi.org/10.1016/j.jmatprotec.2023.117985
Received 27 January 2023; Received in revised form 3 April 2023; Accepted 9 April 2023
Available online 11 April 2023

applications for their alloys in biomedical implants (Lowther et al., 2019).

Given the complexity and cost of powder atomisation, it is often desirable to produce alloys from blended powders in laser powder bed fusion (LPBF), as has been demonstrated for a wide range of alloys that are challenging to manufacture by conventional means, such as Ti-6Al-4V (Simonelli et al., 2018), Ti-50 wt % Ni (Xu et al., 2009), and Ti-25Ta (Soro et al., 2019). This allows a wide range of compositions to be explored rapidly, and the generation of unique microstructural features through localised segregation and changes in melt pool behaviour (Mosallanejad et al., 2021).

It may be desirable to develop noble metal alloys by in-situ alloying. However, where alloying components exhibit significant differences in absorptivity and other thermomechanical properties, guaranteeing uniform consolidation of a blended powder bed is challenging. Whilst increasing incident laser power can improve the quality of melting for noble metals, this is likely to move away from the optimum processing window for other component powders present in-situ alloying. Lack of fusion defects characterised by partially melted particles (Wang et al., 2019) and porosity at low energy densities, followed by a rapid transition to keyhole induced porosity is frequently reported during in-situ alloying (Huang et al., 2021). Alloys of Ti-Ag represent a useful system for investigating this behaviour, given the wide variation in optical behaviour (reflectance at 1070 nm: Ti 0.31 (Johnson and Christy, 1974)), Ag 0.85 (Johnson and Christy, 1972)) and thermal properties (thermal conductivity at 1235 K: Ag 360 (Arblaster, 2015), Ti 15 W m^{-1} K^{-1} (Wilthan et al., 2005)), and the significant interest in generating varied microstructures for antimicrobial response, such as laser engineering net shapes (Maharubin et al., 2019), using spark plasma sintering and acid etching (Lei et al., 2018), as well as the use of nano/micro Ag compounds (Chen et al., 2017). The wide range between the melting points of Ti and Ag (Ti 1668, Ag 962 °C) makes this an extreme scenario that should be extendable to other common alloy matrices such as Fe, Ni, and Co (Fe 1538, Ni 1455, Co 1495 °C). To optimise the initial optical response across a blended Ti and Ag powder bed, tailoring the surface properties of alloy components is necessary.

Over the past few decades, surface coating using physical vapour deposition (PVD) techniques has been of interest in a wide variety of sectors/applications as reviewed by (Kelly and Arnell, 2000), and for generating nanostructures (Behera et al., 2022), nanoporosity (Wadge et al., 2020), and doped-composite surfaces (Coe et al., 2020). Magnetron sputtering has been utilised to generate coatings with tailored structure, composition, thickness, and morphologies, onto various substrate geometries; from 2D discs/plates (Stuart et al., 2015) through to 3D powders (Speidel et al., 2022), scaffolds (Behera et al., 2022), wires (Hanby et al., 2019), and implants (Behera et al., 2022). Although other surface modification techniques exist such as thermal spraying, electroplating, and ion implantation, they face technical limitations compared to magnetron sputtering in the context of coating a powder. For example, fast deposition rates achieved in thermal spray techniques (1–50 μm splats result in coatings >10 μm generally (Herman et al., 2000)) are not ideal for fine control of surface properties whilst minimising coating thickness. Non-uniformity, limited range of compositions, and film cracking/exfoliation are key challenges often observed with electroplating (Fishman et al., 1995). Preparation of metallic core-shell powders has primarily been demonstrated for sintering feedstocks (Li et al., 2019), with most studies detailing thick coatings (> 1 μm) (Ali et al., 2021). Enhancement in the printability of metals via high laser absorptivity coatings is a relatively new field showing promise, but such thick coatings may be detrimental to alloy composition and are not required for changes in absorptivity (Bidulsky et al., 2021). To achieve thin (<1 μm) coatings, with high tailorability through broad material selection, PVD is regarded as one of the most optimal techniques.

The coating of powders using PVD is an established technique for the modification of 3D surfaces of particles (Schmid and Eisenmenger-Sittner, 2013) in the 500 nm to 500 μm range, such as Cu particles with a CrZr coating (2–100 μm Cu particles; (Lassègue et al., 2021)),), Fe particles with an Al coating (2 μm Fe particles; (Kersten et al., 1998)),), and Al_2O_3/WC particles with an Au/Pt coating ($Al_2O_3 \leq$ 500 μm and WC $\leq$ 50 μm; (Ensinger and Müller, 2003)). Applications of these coated powders include next-generation hydrogen storage (Hara et al., 2003), catalysts (Poelman et al., 2007), repurposing of fossil fuel waste products (Xu et al., 2007), as well as the rapidly expanding additive manufacturing sector (Speidel et al., 2022). However, the technique is still not fully optimised for the myriad of feedstock materials in use in research and industry to date. Material type (ceramic, polymeric or metallic), particle size distribution (PSD) and the volume of powder required each provide specific challenges on a case-by-case basis dependent on their intended application.

As PVD is essentially line of sight, the key challenge when coating powders is that the powders need to be manipulated such that all the surface is equally exposed to the flux of sputtered material. This is essential in depositing uniform and homogeneous coatings onto the powder. There are three main approaches investigated in literature for the agitation of powders in the powder container during the process: 1) Rotation (speed, angle, cycle rate, etc.) (Ensinger and Müller, 1994); 2) Vibration (speed, direction, etc.) (Xu et al., 2007); 3) Modified container geometry (Abe et al., 2005).

Similar to previous work (Speidel et al., 2022), an angled (45°) barrel coating rig, developed at the University of Nottingham, was utilised to improve particle agitation. Titanium coatings were applied to silver particles in preparation for use in blended powder feedstocks for LPBF. The influence of two separate deposition conditions (100 W/1 h; 50 W/3 h) were investigated to understand the effect of deposition rate on coating homogeneity and particle agglomeration. Detailed materials characterisation, laser absorptivity and reflectivity of coated powders were assessed. The LPBF build quality of the coated powder blended with Ti powder was compared to blended uncoated powder as a measure of powder performance in manufacture. The key intention of this work is to demonstrate the potential of physical vapour deposition (PVD) to enable homogenously coated powders, and for the first time the use of this coating approach to homogenise the optical response of a blended powder for in-situ LPBF alloying. Alongside demonstrating optimisation of a highly reflective alloying component, the potential to generate new microstructures in the Ti-Ag system offers exciting opportunities for the biomedical community as an established antimicrobial alloy.

2. Materials and methods

2.1. Coated powder manufacture

2.1.1. Pulsed-DC magnetron sputtering

Nitrogen gas-atomised Ag-999 powder (Cookson Precious Metals Ltd) with a nominal particle size distribution of 15–45 μm was used as supplied, with 5 g loaded per run. Coatings were deposited onto the Ag-999 powder using a custom, in-house built University of Nottingham barrel coater. The set-up has been described previously (Speidel et al., 2022), however, a diagram has been included for clarity (Fig. 1). Plasma was generated through a pulsed DC power supply (ENI RPG-50) using two different powers with fixed durations: 50 W for 3 h and 100 W for 1 h (2016 ns pulse width, 150 kHz pulse frequency, 33.5 % duty cycle). Since a shutter is not installed in this equipment due to physical constraints, a high gas flow/pressure (40 standard cubic centimetres per minute (sccm); 1.5×10^{-2} Torr) was used as an alternative to decrease the mean free path of sputtered species as the target cleaning step, reducing risk of coating contamination. After cleaning for 15 min, gas flow was reduced to 10 sccm to achieve a working pressure of 5.5×10^{-3} Torr, nominally chosen as the lowest possible flow rate allowing formation and maintenance of a stable plasma.

Coated powders were subsequently sieved (<106 μm) to remove particles that had agglomerated during the sputtering process. This separated individual coated particles for subsequent processing.

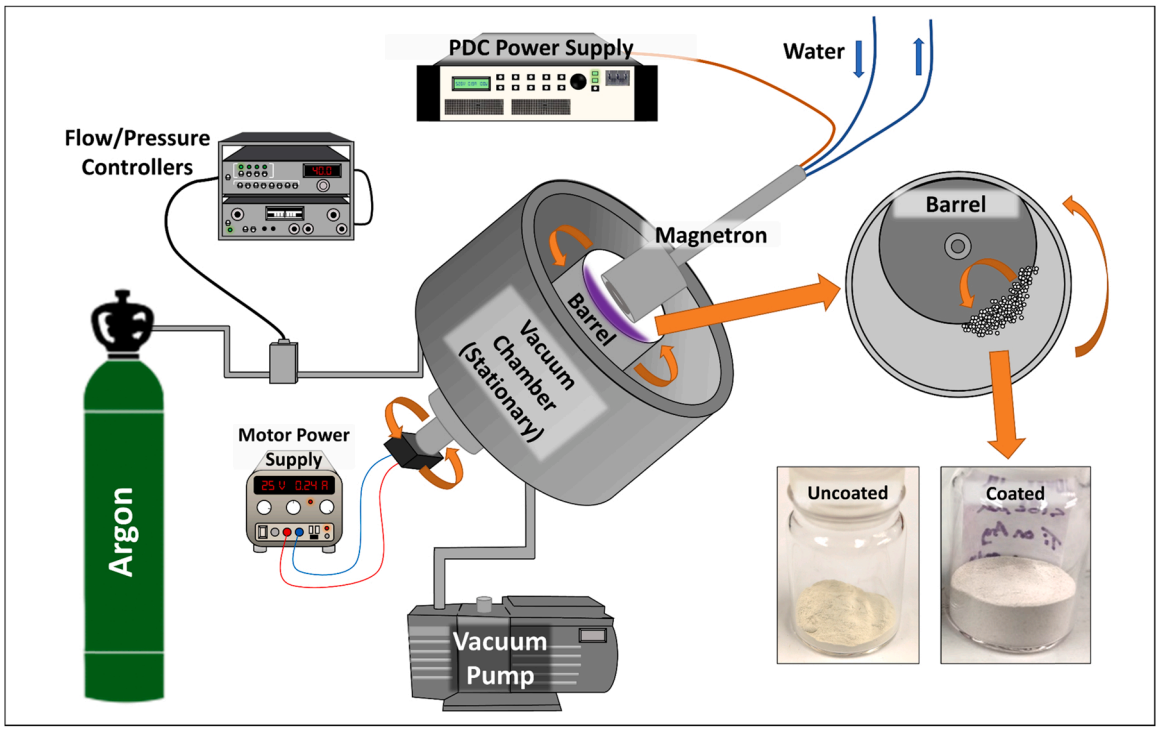

Fig. 1. Schematic diagram of barrel coater PVD setup, illustrating powder tumbling within the barrel and coated vs. uncoated Ag powder.

Illustration of partial agglomeration and differences between sieved (above and below 106 μm threshold), as well as excessive agglomeration are presented in Section 3.2.1.

2.1.2. Coating characterisation

To characterise coating quality, scanning electron micrographs of the loose powder were collected on a Field-Emission Gun Scanning Electron Microscope (JEOL 7100 FEG-SEM). Surface compositional analysis was determined via an Energy-Dispersive X-ray spectrometer (EDS) (Oxford Instruments; working distance 10 mm; beam voltage 15 kV).

X-ray Photoelectron Spectroscopy (XPS) was conducted using a VG ESCALab Mark II X-ray photoelectron spectrometer, with a monochromatic Al Kα source; 30° incident angle. Survey and high-resolution scans were conducted with calibration to 284.8 eV using the C 1s peak. The following processing parameters were used: range 0–1200 eV; step size of 1.0 eV; number of scans set at 2 for survey scans, and 5 for high-resolution scans; dwell time 0.2 s for survey scans, and 0.4 s for high-resolution scans. All data was analysed using CasaXPS.

The diffuse reflectance of prepared powders was characterised via UV–vis–NIR spectroscopy using an Agilent Cary 5000 spectrometer across the UV–vis–NIR spectral range ($\lambda = 200 - 1200$ nm).

2.2. Laser powder bed fusion behaviour

2.2.1. Laser micro calorimetry

To assess melting behaviour of coated powders, laser micro calorimetry (LMC) was performed. In-situ measurements for absorptivity were conducted on a Renishaw AM400 with a continuous wave Yb-fibre laser, operating in modulated exposures at a wavelength of 1070 nm and a spot size of 70 μm. The oxygen content during manufacture was kept below 200 ppm to minimise oxidation during processing. The in-situ absorptivity measurements were conducted as described in previous work (Clare et al., 2020; Speidel et al., 2022) after Trapp et al. (Trapp et al., 2017). The single tracks were deposited onto a 316 L stainless steel disc, machined to a diameter of 10 mm with a thickness of 0.5 mm and a recess depth of 100 μm, to hold the Ag powder layer. The single tracks were 6 mm long and spaced 400 μm apart to allow for a single deposition to be examined at different process parameters. The process parameters used for the absorptivity measurements used laser powers ranging from 120 W to 400 W in increments of 40 W. The laser speed was kept at a constant equivalent speed of 500 mm/s with a point distance of 60 μm and an exposure time of 120 μs.

Single tracks were analysed with focus variation microscopy (FVM). Topographical data, including track volume, width, and continuity, was acquired using an Alicona G4 InfiniteFocus with a 10x objective lens. DigitalSurf Mountains 8 surface imaging and metrology software was used for post processing of the acquired data.

2.2.2. Blended feedstock preparation

To assess the behaviour of Ag powders in a heterogeneous powder bed, powder blends were produced by roller blending. Argon gas-atomised grade 1 commercially pure titanium (cp-Ti) powder with a nominal 15–45 μm size (LPW Technology Ltd) was combined with weighed 25 % ratios of Ag, and sieved 50W_3h coated Ag (cAg), under Ar atmosphere. Powders were blended for 10 h. The resulting blends are referred to as Ti-Ag and Ti-cAg respectively.

Powder size distribution was measured by laser particle size analysis, with water as the dispersant media (Mastersizer M2000, Malvern). A Mie scattering model was assumed, with the refractive indices of Ti used for blended powders as the predominant material by number and volume. To assess particle morphology after blending, backscattered electron (BSE) SEM analysis of as received powder and of blended feedstocks was performed (TM3000, Hitachi). A sample of powder was directly added to an adhesive carbon tab, tapped to remove loose particles, and imaged.

2.2.3. Laser powder bed fusion

Using the blended powders, samples were manufactured by LPBF with a 500 W 1070 nm Yb-fibre laser in an Ar atmosphere (RenAM 500 M, Renishaw Plc). In order to assess response to laser parameters for each material, a parameter spread was generated with variable exposure time and power, with resulting linear energy densities ranging from 133 to 667 J m^{-1}. All other processing parameters were fixed for all studies and based on existing manufacturer optimised parameters for Ti-6Al-4V,

including exposure point distance and hatch distance (90 μm), layer thickness (30 μm), layer angle (67°) and nominal laser spot diameter (75 μm). To minimise powder volume required, samples were manufactured in an undersized reduced build volume (U-RBV) ancillary, with a maximum printing area of 20 × 80 mm and build height up to 10 mm (Supplementary A). Due to the restricted volume of the U-RBV, samples of Ti-Ag and Ti-cAg were produced as 5 mm cubes with 1.5 mm spacing onto a Ti-6Al-4 V substrate.

Sample cross sections were cut parallel to the substrate with abrasive SiC cut-off wheels, and hot mounted in conductive Bakelite (Presidon-ML-C, Aptex Ltd). Samples were ground and polished using an automated rotary preparation machine (Tegramin-25, Struers). For final polishing of samples, activated oxide polishing solution (OP-S) was prepared using colloidal silica suspension (Struers) and 10 vol% H_2O_2 (Sigma). Imaging of microstructures was performed by BSE SEM due to the strong compositional contrast between Ti and Ag (Z = 22, 47).

2.3. Sample nomenclature

For clarity, the naming convention for all samples used in this study, have been compiled in the following reference table (Table 1).

3. Results

3.1. Magnetron sputtering process control

Ag powders showed poor flowability in the coating barrel prior to coating, with the powder 'bulk' sliding and maintaining a position estimated to be ca. 20–40° from the centre-bottom of the barrel. The powder bulk was carried up the edge following the direction of rotation, with the front edge reaching approximately 40° before friction was overcome and the bulk slid back to approximately 20°. In addition to this, the top surface of the powder could be seen 'folding' under the front edge of the bulk (Fig. 2A). Isolated powder particles were also carried up to the top of the barrel and dropped onto the retaining screw and base of the barrel. Due to this, preliminary tests were carried out rotating the powder under vacuum for the two chosen durations; 1 and 3 h, without power applied to the magnetron, to assess the effect of the agitation on the powder. Optical images (Fig. 2B–D), taken after the chamber was vented demonstrated that for both durations, the rotation of the powder caused 'clumps' to form. These were easily broken up with a spatula, but without intervention tended to roll at the front of the bulk, breaking into smaller pieces and reforming periodically.

The coating process resulted in further agglomeration between particles for both deposition conditions, with a significant fraction of material > 106 μm in size (Fig. 4). Despite this agglomeration, improved flow and agitation was observed in both coated 'loose' powders post coating, indicating a change in surface properties. To assess factors in agglomeration, the powder was heated at 60 ± 1 °C for 18 h under low vacuum, prior to coating. The images in Fig. 3 show this result, with the spherical agglomerations missing, instead plate-like agglomerations are present, with a higher proportion of 'loose' coated powder produced. Ultimately, agglomeration persisted irrespective of conditions used.

The agglomeration observed in all conditions necessitated sieving of the coated powders to produce size distributions (>106 and <106 μm) appropriate for LPBF. A low yield per deposition run (ca. 30–40 %) required multiple runs (ca. 15–20) to amass the required amount of powder for subsequent U-RBV analyses. Due to the greater degree of agglomeration observed for the 100W_1h powder, this was prohibitively time consuming and hence was not used in the final builds. Despite the scalability issues raised, there is potential to further optimise the process in subsequent studies to enable higher yields.

Based on these observations, no further deposition conditions were chosen. Reducing the power below 50 W would result in either an unstable plasma, or excessively low deposition rate to generate a suitable coating. Increasing the power above 100 W and the resulting deposition rate would exacerbate the agglomeration issue. As such, in this study only 50 W_3h and 100 W_1h were used as the most suitable comparators.

Table 1
Nomenclature of powders used in this study, with description of their corresponding processing history.

Sample Name	Sample Description
Ag-999	Pure Ag powder
50 W_3h	Ag powder, coated with Ti using the PVD powder coater setup, with magnetron power of 50 W, and deposition time of 3 h. Unless otherwise stated, this powder is sieved to below 106 μm
100 W_1h	Ag powder, coated with Ti using the PVD powder coater setup, with magnetron power of 100 W, and deposition time of 1 h. Unless otherwise stated, this powder is sieved to below 106 μm
Ti-Ag	cp-Ti powder was combined with weighed 25 % ratio of Ag powder
Ti-cAg	cp-Ti powder was combined with weighed 25 % ratio of sieved (<106 μm) 50W_3h coated Ag

3.2. Powder coating characterisation

3.2.1. SEM/EDS

Morphological observations show differences between the uncoated Ag-999 powder (Fig. 5A-B) and the coated alternatives (Fig. 5C–J). For individual particles ca. > 20 μm in diameter, no large difference is noted, aside from increased surface texture that may indicate visible formation of a coating on the surface (Fig. 5B, D, H). Notable differences are seen for particles ca. < 20 μm, with agglomeration of these particles producing rough collective clumps (Fig. 5A, C, G). Bonding between the particles in the agglomerations was seen, demonstrating successful Ti deposition (Fig. 5E, F, I, J). Difficulty, however, in imaging and discerning the Ti coating from the individual Ag-999 powder via SEM was noted, with attempts at sectioning the powder resulted in smearing of the coating with no clear interface.

To help confirm successful coating, EDS (Table 2) was conducted for both the sieved powder sizes (>106 and <106 μm), with Ti being in higher quantities in the < 106 μm powder for the 50W_3h (6.8 vs. 3.8 at %), whilst being lower for the 100W_1h (0.7 vs. 1.6 at%). This agrees with the macroscopic and SEM observations that excessive agglomeration occurred in the 100W_1h powders, whilst the 50W_3h demonstrated better Ti distribution in the non-agglomerated powder. Furthermore, the 50W_3h demonstrated higher Ti content compared to the 100W_1h powders overall, with 6.8 and 0.7 at%, respectively, for the < 106 μm size range. Whilst EDS cannot reliably determine oxygen content, indicative increases in surface oxygen were also noted relative to the Ag-999 powder, increasing from 0 to 33.9 and 12.5 at% for the 100W_1h and 50W_3h powders, respectively. Again, the lowest oxygen content was found for the 50W_3h (<106 μm) powder, demonstrating the optimal condition of those tested.

Despite the observed agglomeration, it was clear the lower deposition rate/longer deposition time combination (50W_3h) resulted in better overall coating of the powder both visually (optical and SEM) and chemically (EDS).

3.2.2. XPS

XPS analyses of native Ag-999 powder, as well as both of the Ti-coated powders (50W_3h and 100W_1h) are detailed in Fig. 6(A–C) & Table 3. Survey spectra for all powders are presented in Supplementary B, detailing all peaks present for the powders tested. For the Ag-999 powder, O 1s (Fig. 6A) demonstrated two peak components located at 531.7 eV (48.1 %) and 534.1 eV (51.9 %) likely corresponding to residual surface oxygen and water, respectively (Boronin et al., 1998). As expected, no Ti 2p peak was seen for the native Ag-999 powder (Fig. 6B). For the Ag 3d doublet peak (Fig. 6C), two peaks were present with a Δ_{eV} of ca. 6 eV. The 3d 5/2 peak was located at 368.6 eV, which is likely Ag (0) (Galindo et al., 2013).

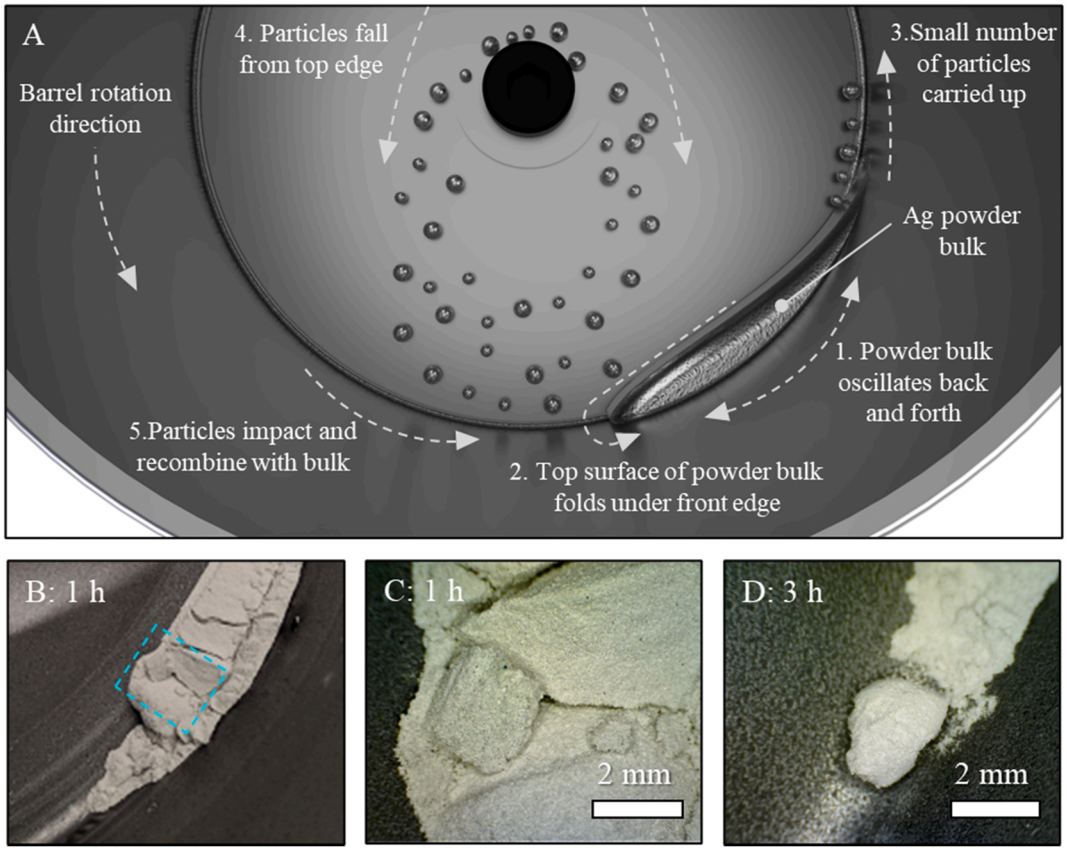

Fig. 2. A) Schematic demonstrating the motion of the powder bulk and isolated particles (not to scale) in the powder barrel during coating, the powder flows over the top surface of the bulk, folding under the front edge, with particles carried up and dropped down to recombine. Photograph B and Optical microscope images C and D of Ag-999 powder after 1 and 3 h barrel rotation, without power applied to the magnetron to assess the effect on agglomeration. Region indicated in B corresponds to image in C.

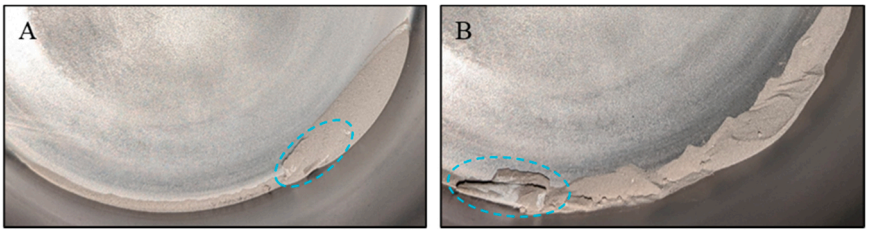

Fig. 3. Representative macroscopic photos of a 50W_3h coating process which included a heated drying step. Photo A, undisturbed powder bulk, B, after separation with a spatula, plate-like agglomerations are present as opposed to spherical agglomerations. The obscured, and then separated agglomerations are highlighted in cyan.

Following Ti coating, both the 50W_3h and 100W_1h powders demonstrated similar peak components for the O 1s (Fig. 6A), Ti 2p (Fig. 6B), and Ag 3d (Fig. 6C) high resolution spectrums. O 1s spectrums detailed two peak components, with a shift (ca. 1.5–1.9 eV) to lower binding energies for both components, which were characteristic of metallic oxide and hydroxides or sub-surface oxide for Ti (Dupin et al., 2000). Specifically, the 50W_3h powder had peaks and relative peak ratios of 530.1 eV (75.5 %) and 532.2 eV (24.5 %), whilst the 100W_1h powder exhibited peaks at 530.2 eV (70.1 %) and 532.2 eV (29.9 %). Both powders detailed a 2p doublet peak for Ti, with a Δ_{eV} of 5.4 eV, Ti 2p3/2 peak positions located at 458.7 and 458.5 eV for 50W_3h and 100W_1h, respectively, corresponding to Ti^{4+} (TiO_2) (Wadge et al., 2020). The Ag 3d high resolution doublet peak demonstrated a subtle (ca. 0.4 eV) shift to a lower binding energy for both Ti-coated powders, however, the Δ_{eV} remained constant, which corresponded to Ag(0).

Table 3 details the total elemental compositions of the tested powders quantified from the survey spectra (Supplementary B) via CasaXPS. As can be seen, the Ag-999 powder surface contains only Ag and O at 73.4 and 26.6 at%, respectively. Following Ti-coating, both the 50W_3h and 100W_1h powders demonstrated increases in Ti and O content, similar to EDS (Table 2), with a drop in Ag, with Ag, O and Ti quantities of 23.5, 59.2, and 17.4 at%; and 34.4, 50.0, 15.6 at%, respectively.

3.3. Laser powder bed fusion and optical response

3.3.1. UV–vis–NIR

Diffuse reflectance of the powder samples was measured across the UV–vis–NIR spectral range (200 – 1200 nm) (Fig. 7A). All spectra are characteristic of Ag in this range with a strong UV absorption peak (ca. 320 nm) and high reflectance in the vis-NIR regions (>400 nm). The deposition of Ti reduces apparent reflectance at 1070 nm (Yb-fibre laser

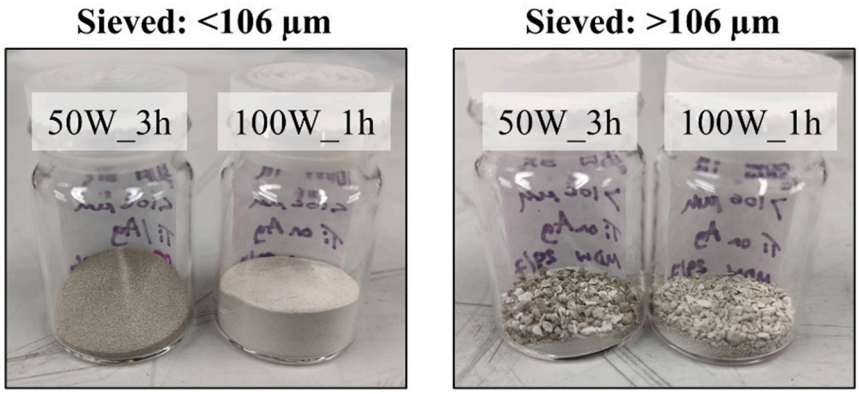

Fig. 4. Representative macroscopic images of powder samples (multiple batches) subjected to 106 µm sieving (above and below the sieving threshold), with < 106 µm used for further processing, to illustrate optical and morphological differences. Quantity shown not indicative of final quantities generated.

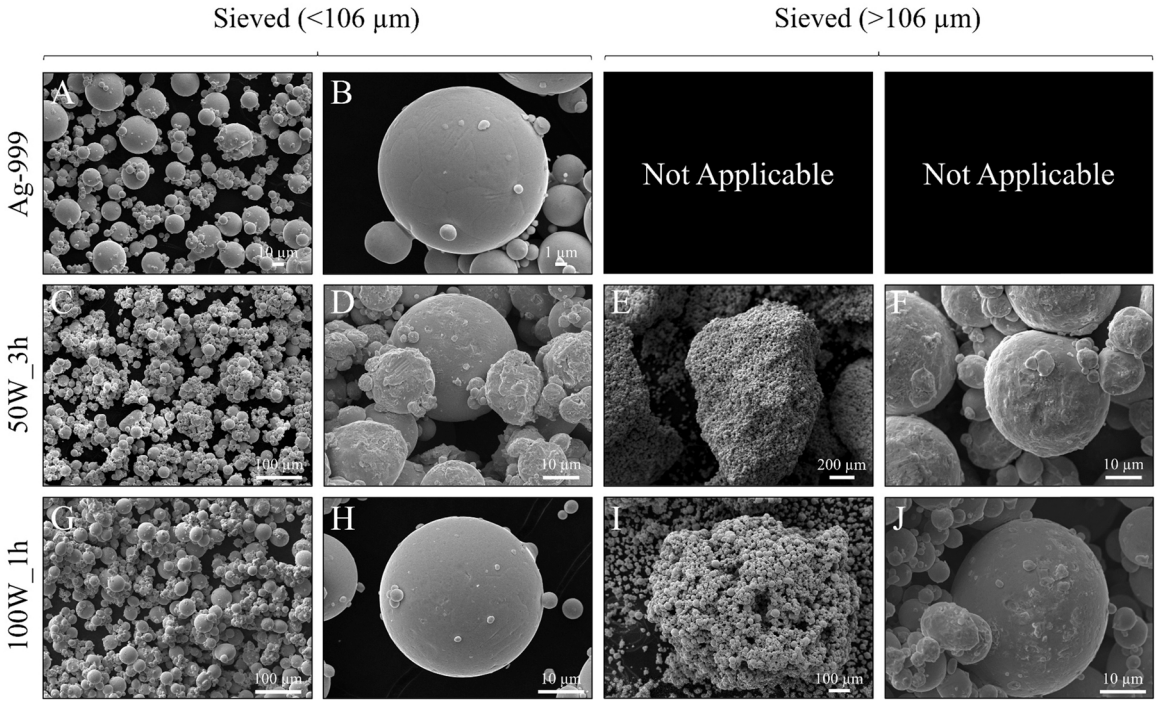

Fig. 5. SEM micrographs detailing surface features of the uncoated (Ag-999; A & B) and coated (50W_3h; C-F, and 100W_1h; G-J) powders. Images A, B, C, D, G, & H) are sieved < 106 µm, whilst E, F, I & J) are sieved > 106 µm.

Table 2
EDS elemental compositions of all powders tested: Ag-999 powder, 50W_3h, and 100W_1h. All values are given as mean with standard error (n = 5).

Sample ID	Elemental Composition/at% (EDS)		
	Ag	O	Ti
Ag-999 Powder	100	0	0
50W_3h (<106 µm)	80.7 ± 0.6	12.5 ± 0.5	6.8 ± 0.1
100W_1h (<106 µm)	65.5 ± 0.3	33.9 ± 0.2	0.7 ± 0.1
50W_3h (>106 µm)	59.1 ± 0.4	37.1 ± 0.2	3.8 ± 0.2
100W_1h (>106 µm)	63.4 ± 0.1	34.9 ± 0.1	1.6 ± 0.1

wavelength), where the reflectance of Ag-999 is 60 %, reducing to ca. 46 % for the 100W_1h sample and ca. 35 % for the 50W_3h powder.

3.3.2. Single track deposition behaviour

3.3.2.1. Focus variation. Fig. 7B shows the track morphology as measured by FVM of Ag-999, 50W_3h and 100W_1h respectively. At low laser powers, all three powders show balling defects, with the pure Ag powder showing significant track disruption. Clear differences can be seen between all material types. The pure Ag tracks all feature irregularities such as balling and discontinuities during the track length, with continuous tracks formed only between 320 and 400 W. The 50W_3h powder shows improved track continuity to the pure Ag tracks, with continuous tracks from 280 to 400 W, and 400 W tracks appearing much more stable. The thickness of 50W_3h tracks (175 µm at 400 W) is reduced compared to both the pure Ag (235 µm) and the 100W_1h (220 µm) powders. The 100W_h powder shows improved track continuity, with continuous tracks at 200 W, compared to the 320 W/280 W of the pure Ag and 50W_3h tracks respectively. Track width for the 100W_1h is larger, with a thick continuous track 220 µm wide produced at 400 W.

3.3.2.2. Absorptivity. Fig. 7C shows absorptivity as a function of laser power. At 160 W and above, there is an increase in absorptivity, peaking

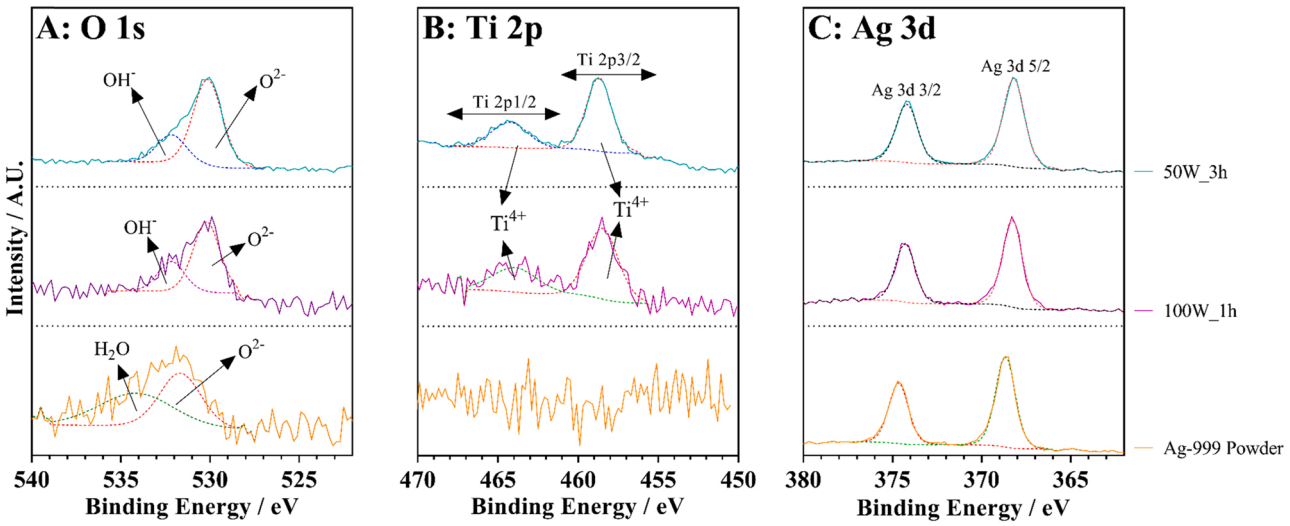

Fig. 6. High-resolution XPS spectra detailing differences in Ag-999 powder following Ti magnetron sputtered coatings (50W_3h & 100W_1h). A) O 1s XPS high resolution spectra; B) Ti 2p XPS high-resolution spectra; C) Ag 3d XPS high-resolution spectra. Dashed lines represent fitted peak components.

Table 3
XPS elemental compositions of all powders tested: Ag-999 powder, 50W_3h, and 100W_1h. All values are given as mean with standard deviation as calculated through CasaXPS, normalised to carbon.

Sample ID	Elemental Composition/at% (XPS)		
	Ag	O	Ti
Ag-999 Powder	73.4 ± 4.1	26.6 ± 3.7	0
50W_3h	23.5 ± 0.5	59.2 ± 1.0	17.4 ± 0.8
100W_1h	34.4 ± 2.0	50.0 ± 2.8	15.6 ± 2.6

at 0.44 for the 50W_3h powder, 0.39 for the 100W_1h powder, and 0.31 for the pure Ag powder. Both coated powders have increased the absorptivity from the pure Ag powder at all laser powers. At low laser powers, the 50W_3h powder increases the absorptivity of the pure Ag powder (0.22 at 160 W) by 31 %, whereas the 100W_1h powder increases the absorptivity by 18 %. At 320 W the largest difference can be seen, with the 50W_3h powder increasing absorptivity by 62 %, whereas the 100W_1h powder increases the absorptivity by 18.5 %. Both pure Ag powder and the 100W_1h powder steadily increase in absorptivity as the power increases, without deviating much at higher powers. However, the 50W_3h powder steadily increases at an increased gradient, peaking at 0.44 (320 W), before dropping to 0.32 at the maximum 400 W power, which may indicate vaporisation of Ag is occurring. Crucially, at the minimum laser power, the absorptivity of 50W_3h is enhanced to a higher level than observed for all uncoated Ag tracks.

3.3.3. *Powder blending*

Prior to the final LPBF manufacture, all powder types were analysed for particle size distribution (Ag, Ti, coated and sieved Ag (cAg), 25 wt % Ti-cAg and Ti-Ag). The PSD of as-received feedstock, sieved coated powder, and powder blends show broad agreement with the nominal 15–63 μm size range that is commonly used for LPBF (Fig. 8).

The sieved coated Ag powder (cAg) exhibits a bimodal distribution, with a secondary peak centred at 250 μm, indicating some sieve bypass or post sieve agglomeration has occurred. This accounts for 4.2 ± 1.1 % by volume of the powder. Upon blending with Ti powder, further agglomeration occurs, with a resulting 8.3 ± 0.8 % outside of the 106 μm sieving range.

Post blending agglomerates are present in both Ti-Ag and Ti-cAg (Fig. 8D and E). The presence of Ti fines in both of these agglomerates confirms that agglomeration occurs during the roller blending process. The absence of compositional contrast within individual cAg particles under backscattered electron imaging indicates that the Ti coating layer is uniform and has not undergone spallation during blending (Fig. 8E).

3.3.4. *Blended powder LPBF*

Following LPBF, significant porosity is observed for Ti-Ag at low energy density (Fig. 9A). These pores follow the shape of surrounding particles, indicating that they are caused by a lack of fusion and not keyholing. The internal surfaces of these pores are rich in silver, as indicated by the relative brightness under BSE. In comparison, Ti-cAg shows notably lower visible porosity (0.2 % vs 3.9 % at 167 J m^{-1}) (Fig. 9B).

Large regions of segregated Ag-rich phase are also apparent in the Ti matrix at low linear energy density (167 J m^{-1}). This reduces as energy density increases, with only isolated regions of segregation remaining at 667 J m^{-1} (Fig. 9C). These isolated regions are likely associated with the larger Ag agglomerates identified in the powder blend given the similar dimensions. Use of cAg powder results in greater retention of micro-segregation, as apparent from the visibly larger total area of bright Ag rich regions (Fig. 9D).

Within individual Ag or Ti rich regions of Ti-Ag and Ti-cAg, no significant differences in microstructure are observed. Spherical 15–45 μm pockets of Ti rich phase are entrained in larger 200 μm agglomerations of silver (Fig. 9E). Retained silver rich phase does not exhibit the same geometry as Ag agglomerations observed in the powder, indicating these are not lack of fusion defects. A dendritic microstructure is apparent in silver rich regions (Fig. 9F). Point measurements by EDS indicate that Ag rich regions are not intermetallic in nature, with typical compositions of ca. 80 at% Ag (Supplementary C).

Across the entire range of energy densities explored (133–667 J m^{-1}), Ti-cAg retains at least 3 % segregated Ag rich regions by imaged area (Fig. 10A). Additional to segregation, porosity as a function of blending Ti and pure Ag or coated Ag in their respective builds was quantified. A notable reduction in porosity at energy densities below 500 J m^{-1} is observed for Ti-cAg (0.3 ± 0.6 % vs 4.2 ± 2.8 %). As energy density increases, improved consolidation is observed, alongside greater homogenisation of the Ti-Ag microstructure.

4. Discussion

Modifying high reflectance powders for LPBF has seen great improvements in recent years, through various methods, most notably CrZr (Lassègue et al., 2021) and Zn (Speidel et al., 2022) coatings on Cu particles, as well as others reviewed by Bidulsky et al. (Bidulsky et al.,

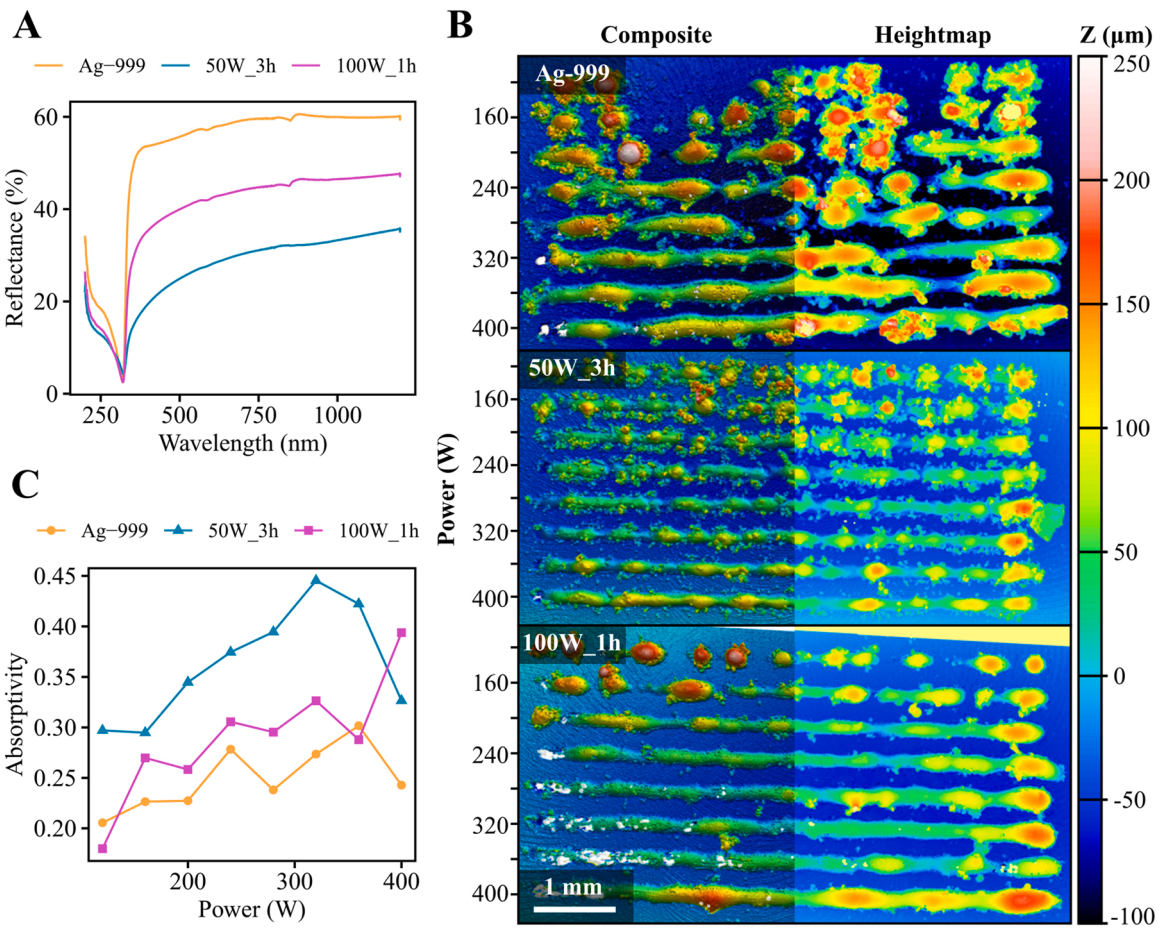

Fig. 7. A) Diffuse reflectance measurements of the pure Ag, 50W_3h and 100W_1h powders across the UV–vis–NIR spectral range (200–1200 nm). B) Single track morphology as measured by the FVM of the pure Ag, 50W_3h and 100W_1h laser microcalorimetry samples. Composite track profiles alongside heightmap data are shown. C) Laser absorptivity as a function of laser power for the same samples described.

2021). This study details the modification using magnetron sputtered Ti coatings to improve absorptivity, and reduce reflectivity, of difficult-to-process Ag-999 powder. Despite the small scale, preliminary assessment made in this study, the technique offers significant scalability to generate sufficient quantities of coated powders for L-PBF (Florando, 2006). Titanium was chosen in particular as Ti and Ag exhibit a wide divergence in optical and thermal properties, whilst being broadly miscible across the Ti-Ag phase diagram with alloys of interest for their antimicrobial properties. By utilising the improved absorptivity of a Ti coating to enable appropriate melting of Ag, it may be possible to generate unique alloys by in-situ powder bed alloying of blended Ti-Ag powders whilst achieving good consolidation of the resulting material. This is an especially promising result in a biomedical context given that Ti-Ag alloys have been shown to exhibit antimicrobial behaviour (Shi et al., 2020).

Silver powders suitable for LPBF present challenges for intermediate processing steps. Their high density (10.49 g.cm^{-3}), and in this study fine particle size (< 20 µm), inherently reduce flowability (Clayton, 2019). Particle size is a well-established factor in powder cohesion, with the increased surface area of finer particles inducing agglomeration (Meier et al., 2019a). This is one likely reason for agglomeration observed in this study, alongside the resulting poor flow and agitation in the barrel (Fig. 2*A*). The influence of particle size has been previously explored focussing on a Zn coating of two sized Cu powders: < 45 and < 63 µm, with the smaller particle size demonstrating poor uniformity of coating due to similarly poor flow. However, no agglomeration was noted in either powder size, and hence suggests there may be a critical metric relating powder diameter and density with non-uniform deposition, and eventually agglomeration, due to poor flow (Knieps et al., 2021). One aspect that is clear is that irrespective of coating technique, Ag powder will ultimately agglomerate given any mechanical agitation. Prior to this study, we tested a bespoke mechanical separator which acted as a rake for the powder, however, this again resulted in agglomerations and hence was not taken further. It was seen that tumbling under vacuum alone, without applying a Ti coating, resulted in clumping of the powder, which tended to roll at the front of the bulk, breaking into smaller pieces and reforming periodically during rotation. Despite trailing various methods to prevent particle agglomeration prior to Ti deposition, including different barrel geometries and rotation speeds (data not shown, study utilised optimised conditions), clumping of the powder was still seen, which further confirms the inherent cohesiveness of the Ag powder as received. This phenomenon was exacerbated by the deposition of Ti coatings as the clumps formed within the barrel, Ti atoms condense onto these aggregates during deposition. If the flux was too high, this would cause the clumps to be encapsulated before the leading edge of the powder caused break up. This may explain the larger agglomerates seen for the higher power (Fig. 5I). Ultimately, this phenomenon is further exacerbated by the applied coating as it encapsulates the produced agglomerations, especially depending on the technique used. Despite these observed technical challenges, magnetron sputtering is still a preferred coatings methods for this type of applications since deposition rate can be finely tuned to enable thin coating of the powders, without adding to the agglomeration. Other techniques, such as thermal spray (Herman et al., 2000) are not ideal for fine control of surface properties whilst minimising coating thickness. Furthermore, when considering electroplating (Fishman et al., 1995), non-uniformity of

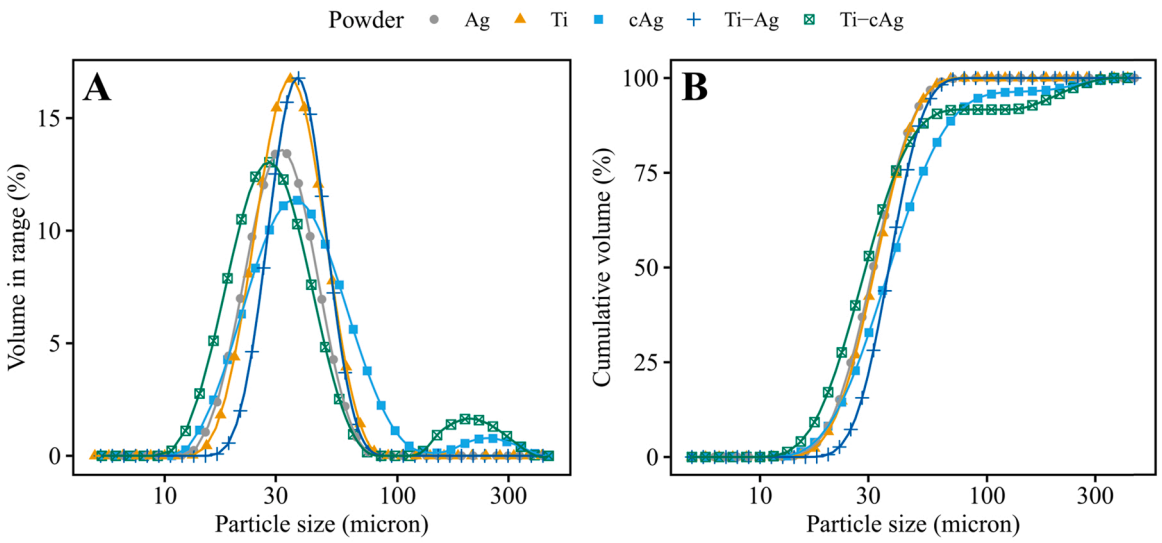

C	D10 (µm)	D50 (µm)	D90 (µm)	< 15 µm (vol%)	> 45 µm (vol%)	> 106 µm (vol%)
Ag	20.6 ± 0.1	31.5 ± 0.1	48.1 ± 0.2	0.8 ± 0.1	14.0 ± 0.3	0
Ti	21.2 ± 0.4	32.2 ± 0.6	48.6 ± 1.0	0.5 ± 0.1	14.8 ± 1.5	0
cAg	20.8 ± 0.3	37.4 ± 0.8	72.9 ± 5.5	1.3 ± 0.3	35.3 ± 2.2	4.2 ± 1.1
Ti-Ag	26.1 ± 0.2	37.1 ± 0.3	52.4 ± 1.5	0	23.5 ± 2.2	0
Ti-cAg	17.6 ± 0.1	29.3 ± 0.1	58.6 ± 2.3	3.9 ± 0.1	17.7 ± 0.2	8.3 ± 0.8

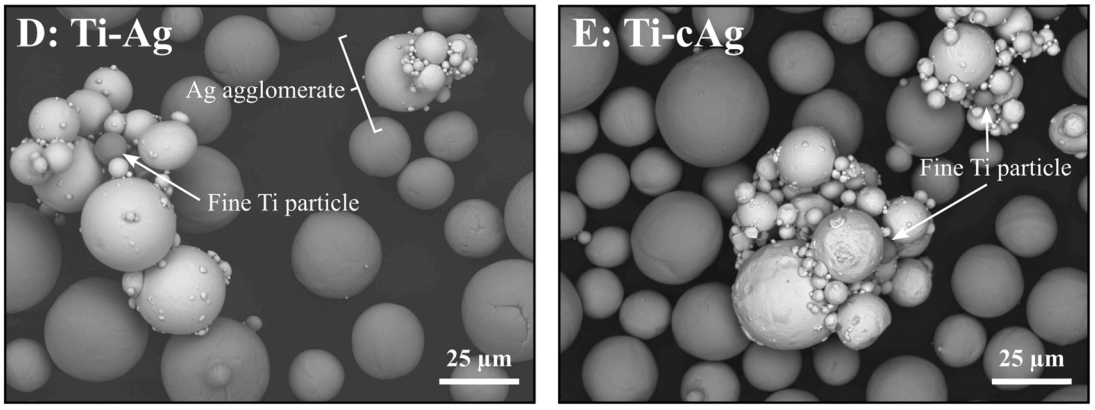

Fig. 8. Particle size analyses of feedstocks, with A. volume distribution, B. cumulative volume shown for each feedstock, and C. key sample statistics for each powder. SEM images of agglomerates in D. Ti-Ag and E. Ti-cAg are shown, with Ti fines present in both.

coating, limited range of compositions that can be applied since there is a requirement for metallic solutions to generate ions for coating, and film cracking/exfoliation are key limitations, which are not observed in magnetron sputtering.

Alongside bulk properties of the alloy, the surface behaviour of particles play a significant role in agglomeration. Oxide films act to reduce the cohesive surface energy of metal powders (Meier et al., 2019b), and as established by EDS measurement, the as-received Ag-999 powder has no appreciable surface oxide (Table 2). The nobility of Ag may induce adhesion due to the lack of a passive oxide surface film, which may lead to cold welding of the Ag powder (Akande et al., 2010). However, the comparatively weak vacuum used during sputtering (5.5×10^{-3} Torr) is unlikely to support this process (Merstallinger et al., 2009).

Moisture content on the powder particle surface could also contribute to the difficult processing. Abe et al., worked under the assumption that moisture was not a contribution in their study on particle size and shape effects during coating (Abe et al., 2004). In contrast to this, the authors believe moisture may still be a significant factor in the agglomeration seen, however, this phenomenon is likely multifactorial. Further to understanding the effect of tumbling the powder alone, and tumbling the powder followed by coating, an additional drying step under vacuum prior to coating was assessed (Fig. 3). This condition still resulted in agglomerations, which were plate-like compared to spherical agglomerations seen through just tumbling, indicating that the rolling of roughly spherical agglomerates at the front edge had not occurred. The fact agglomeration was still seen, suggests that additional factors beyond moisture are likely present in this process.

From the two deposition conditions used, the 50W_3h deposition resulted in a reduced incidence of larger agglomerates, with higher quantities of Ti, as confirmed by EDS (Table 2; 17.4 and 15.6 at%, respectively) and XPS (Table 3; 6.8 and 0.7 at%, respectively), deposited onto individual, or small clusters (<10 particles) as compared to the 100W_1h samples (Fig. 5). This result is likely due to the lower

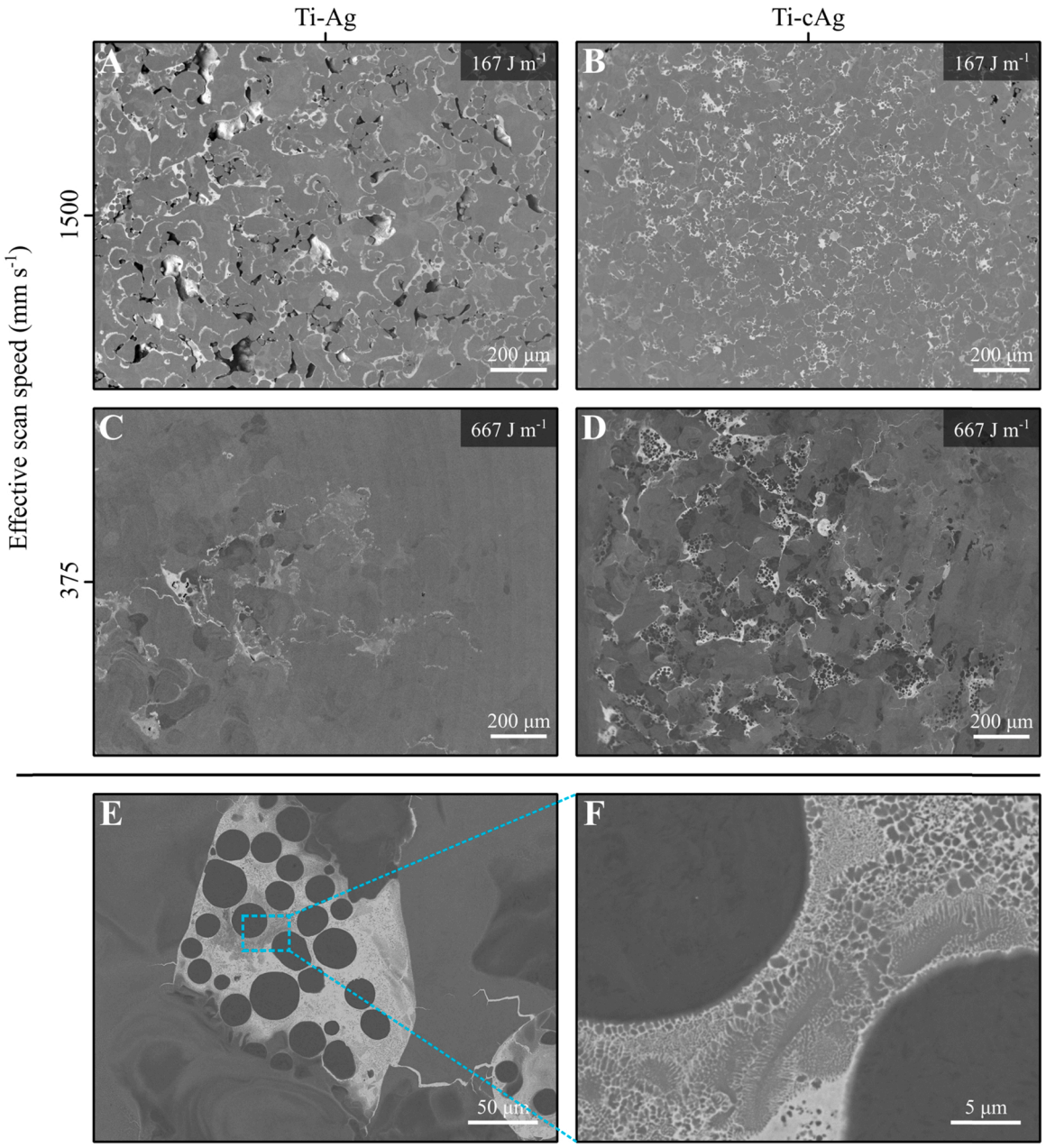

Fig. 9. Example micrographs (A–D) show the variation in microstructural characteristics for Ti-Ag and Ti-cAg in the X-Y plane. Higher magnification image (E) shows the presence of spherical Ti pockets within the Ag rich regions, and inset (F) the dendritic microstructure of the Ag rich zones.

deposition rate allowing enough time for the clumps to break up before fully encapsulating them. Once a critical number of the particles had some Ti deposited onto the surface, the change in surface composition reduced the tendency to agglomerate described above, resulting in individual particles or smaller clusters being coated. The improved flow behaviour of the non-agglomerated powder post–coating suggests this. The surface of the coated powders appeared consistent morphologically, with smooth, homogeneous Ti deposition on both of the < 106 µm powders (Fig. 5). Both the 50W_3h and 100W_1h powders exhibited oxygen inclusion in the films (Table 2 & Table 3), as Ti rapidly passivates on atmospheric exposure when removed from the coating rig. It is important to minimise oxygen inclusion, as formation of oxide surfaces is known to inhibit or disrupt the LPBF process due to oxide films having significantly different absorptivity properties compared to the pure metal/alloy counterparts. Ultimately, this can result in combinations of poor powder melting, poor consolidation, and increased porosity (Ohtsuki et al., 2020). However, as the surface O content measured by XPS (Table 3 & Fig. 6) is in proportion to the Ti content measured, no additional oxidation of Ag has been caused by the coating process and a stable coating has been formed.

Regarding the application of these coated powders in additive manufacturing via LPBF, the optical response is key to assess. UV–vis–NIR spectrophotometry (Fig. 7A) demonstrated a marked reduction in diffuse reflectance compared to the pure Ag-999 powder at the 1070 nm wavelength (34 % and 47 % for 50W_3h and 100W_1h, respectively, compared to 60 % for Ag-999; Fig. 7). This reduction in reflectance is likely driven by two mechanisms. First, the higher absorptivity of Ti compared with Ag (Fig. 7C), coupled with the oxidation of the Ti surface under ambient conditions to TiO_2. This effect causes the reduction in the gradient between 320 and 400 nm in the Ti-coated powders, noting that TiO_2 absorbs strongly within this region (Kudo et al., 2018). Second, the reduction in reflectance could be correlated to

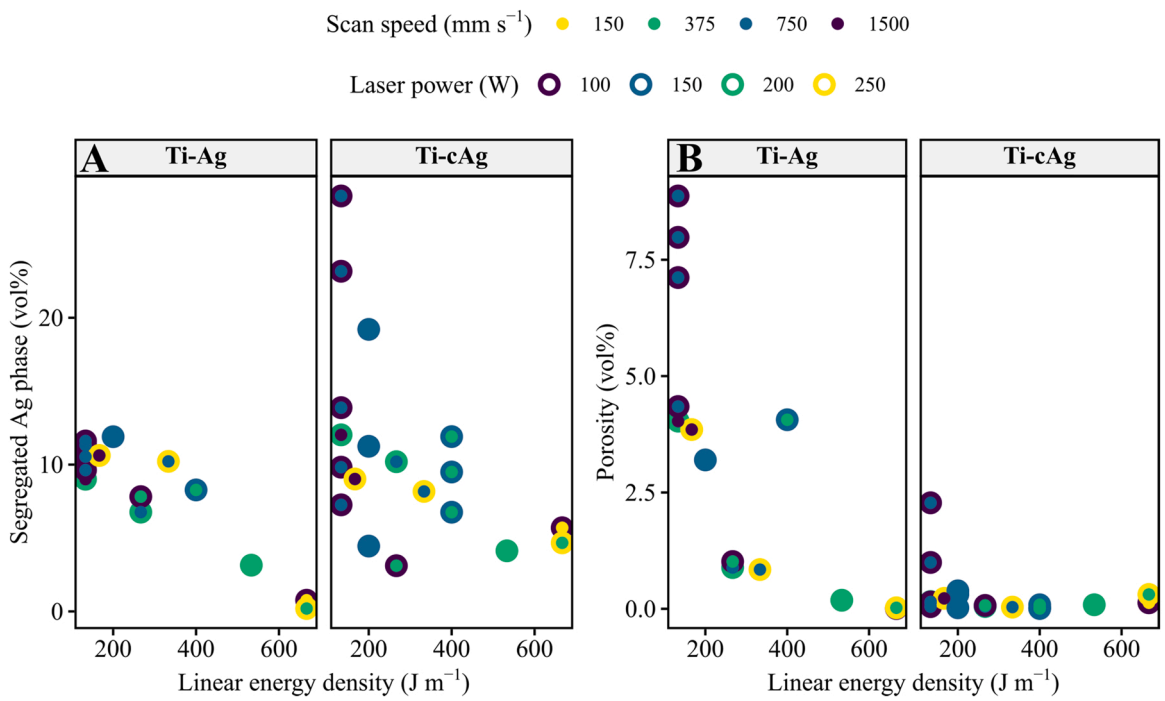

Fig. 10. A) Microstructural segregation and B) porosity of Ti-Ag and Ti-cAg calculated from image analysis of SEM. Similar trends are observed of decreasing segregation and porosity as energy density increases. Colour scale of points represent the respective scan speed (inner point) and laser power (outline).

increased scattering from the agglomerated powder versus the discrete particles of the virgin supply condition (Fig. 5). Measurement by UV-Vis-NIR provides the diffuse reflectance across a large area of powder and is therefore sensitive to bulk morphological effects.

Similarly, the absorptivity (Fig. 7C) as measured by single-track LMC (Fig. 7B) increased due to both powder coatings, rising by 19 % and 62 % relative to Ag-999 for the 100W_1h and 50W_3h powders, respectively, at 320 W. The incidence of continuous track lengths occurred at significantly lower powers for the coated powders, with continuous tracks seen at 200 and 280 W for the 100W_1h and 50W_3h, respectively, compared to the Ag-999 at 320 W. This clearly demonstrates that the addition of Ti coating has improved the likely manufacturability of the powders, and that the optimum coating conditions at 50W_3h result in the greatest improvement in manufacturability.

Considering these results in detail, samples exhibit lower absorptivity (Fig. 7C) than is implied by reflectance measured by UV-Vis-NIR at 1070 nm (Fig. 7A), assuming all non-reflected radiation is absorbed. Measurement by UV-Vis-NIR is performed without any melting or phase change, and is dependant only on the uppermost surface layer, surface morphology, and packing of the powder in the sample holder. In contrast, in-situ absorptivity calculated through LMC (Fig. 7B-C) details the net absorptivity for the whole scan track, including both initial interactions between laser and powder through to a fully developed melt pool. The low reflectance of 50W_3h compared to uncoated Ag implies that initial melting will be rapid in LMC, resulting in a faster transition to a melt pool. Once this occurs, coupling with the laser is enhanced and the proportion of incident energy transferred to heat is improved. As a result, the time-averaged absorptivity across this process is increased, despite the anticipated short life-time of the solid Ti coating layer. This phenomenon has previously been observed by Clare et al., wherein material absorptivity is highly dependent on melt pool geometry (Clare et al., 2020). This behaviour also contributes to the overall increase in absorptivity as incident laser power increases, with recoil pressure causing depression of the melt pool surface. This in turn increases the mean number of reflections for a given incident photon, further increasing the likelihood of absorption and an effective increase in absorptivity. It is important to note that whilst LMC has advantages in providing a measurement of absorptivity that includes melting behaviour, a high sensitivity to layer thickness means that results cannot be directly extrapolated to printing behaviour but are instead indicative of laser interaction.

Crucially, the addition of Ti coating drastically improves consolidation of the Ti-Ag microstructure in L-PBF at lower energy density (Figs. 9 & 10). The ability to manufacture across a wider range of energy densities provides several potential benefits. By giving access to tailor both laser power and scan speed, processing parameters can be chosen that lie closer to existing optimised scan strategies for Ti alloys (Buhairi et al., 2022). This avoids both porosity through incomplete densification, and the formation of keyhole pores through excess incident laser energy. Given the demonstrated improvement of absorptivity for cAg, this is likely to be the dominant factor. Considering an individual laser exposure striking a silver rich region of the powder bed, the effective energy input will be dominated by the reflectivity of the particles. As segregated Ag present in both Ti-Ag and -TicAg does not follow the original shape of Ag particles in the blended powder, it is reasonable to assert that Ag was melted in both cases. However, by increasing absorptivity, greater thermal input will result in improved melting of both Ag and adjacent Ti particles, and therefore improved densification (Fig. 11).

This model correlates with observed microstructural features in SEM (Fig. 9). The surface of pores within the Ti-Ag matrix appears coated with a layer of silver, indicating that any Ag melt has wet adjacent Ti particles, but without sufficient energy input to allow either molten Ti or Ag to fill the pore before solidification. The apparent segregation of Ti and Ag has previously been observed in melt-spinning of Ti-Ag-Cu alloys, with a miscibility gap present at the extreme cooling rates expected in LPBF (Ziewiec et al., 2009). Upon heat treatment, this segregation may enable precipitation of Ti-Ag intermetallics in greater volumes than could be achieved in a homogeneous Ti-25Ag alloy. These intermetallic phases, in particular Ti_2Ag, have been associated with enhanced antimicrobial response in Ti-Ag alloys (Chen et al., 2017), and this principle of localised segregation for unique non-homogeneous alloys may have applications in other fields where local anisotropy of material is beneficial, as explored in metal matrix composites (Chawla, 2012). Addition of segregated silver may have particular benefits in improved

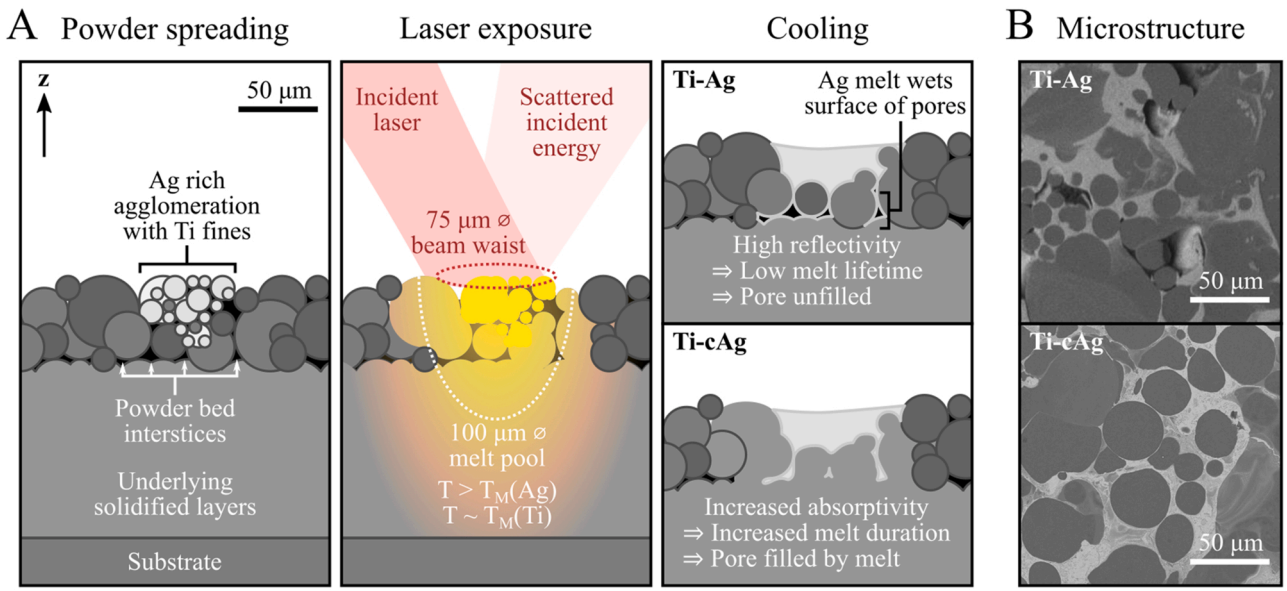

Fig. 11. A Schematic of the melting process in a mixed Ti-Ag powder bed, and B resulting microstructure for Ti-Ag and Ti-cAg.

tribological properties (Tyagi et al., 2011). A thorough mechanical characterisation of any developed alloys will be necessary, both to assess the mechanical performance as manufactured and how subsequent microstructural development alters this.

It remains unclear why the addition of Ti coating reduces interdiffusion of Ti-Ag during in-situ alloying at high energy densities. This could be linked to the previously discussed change in reflectivity as particles transition to a planar melt pool, however significant further study would be required to confirm this. High resolution in-situ melt pool monitoring, coupled with extensive microstructural investigation of single track and bulk samples may be able to elucidate this (Lane et al., 2020).

One key concern for manufacturing with blended powders is the risk of spread-induced de-mixing during the LPBF process. Variations in particle size can induce de-mixing (Mussatto et al., 2021), and the deposition of larger particles at the end of recoating motion has been demonstrated in both computational modelling (Phua et al., 2021) and physical experiments (Shaheen et al., 2021). Due to the limited volume of powder available in this study, the repeated prints necessary to establish variations in composition caused by de-mixing were not possible. However, visual observation of excess powder at the end of each recoater sweep did indicate an increased content of Ag particles. With improved process control to minimise agglomeration through optimal drying, agitation (vibration, rotation speed, etc.), deposition parameters, it may be possible to use the coating process to improve the flow behaviour of blended powders, with the resulting uniformity of surface energy across all component powders.

Alongside demonstrating the improved manufacturability of blended Ti-Ag powders with surface coating, this work has implications for improving the manufacturability of bulk Ag via LPBF. As indicated by LMC, stable melt tracks can be produced at lower input energy with coated Ag powders (Fig. 7B). It may therefore be possible to enhance the manufacturability of noble metals, whilst retaining their unique thermal and optical properties with minimal alloying caused by the surface coating. Improving the yield from the PVD process used in this study will be key to achieving this.

5. Conclusions

In this work, the optical response of reflective silver powders was successfully tailored through a sputtered Ti coating. Agglomeration of Ag particles was found to occur independent of sputtering, however this phenomenon was exacerbated at higher deposition rates corresponding to higher sputtering power (100 vs. 50 W). The control of powder flow within the processing barrel remains a key performance indicator for successful coating. Superior melting performance was demonstrated for the coated powders during both single-track melting, and when used as a component in blended Ti-Ag powder for in-situ LPBF alloying, with reduced porosity (0.3 ± 0.6 % vs 4.2 ± 2.8 %) and a wider range of melting strategies accessible. Through further optimisation of the flow performance of input powders and possible vibration of the sputtering chamber, there is a promising route to the optimisation of challenging alloys for high-value additive manufacturing, such as in bespoke, medical device design.

CRediT authorship contribution statement

Dr Matthew Wadge: Conceptualization, Methodology, Validation, Formal analysis, Investigation, Resources, Data curation, Writing – original draft, Writing – review & editing, Visualization, Supervision, Project administration, Funding acquisition. **Dr Morgan Lowther:** Conceptualization, Methodology, Validation, Formal analysis, Investigation, Resources, Data curation, Writing – original draft, Writing – review & editing, Visualization, Supervision, Project administration. **Timothy Cooper:** Conceptualization, Methodology, Validation, Formal analysis, Investigation, Data curation, Writing – original draft, Writing – review & editing, Visualization. **Dr William Reynolds:** Methodology, Validation, Formal analysis, Investigation, Data curation, Writing – original draft, Writing – review & editing, Visualization. **Dr Alistair Speidel:** Validation, Formal analysis, Investigation, Data curation, Writing – original draft, Writing – review & editing, Visualization. **Dr Luke Carter:** Conceptualization, Methodology, Validation, Formal analysis, Investigation, Resources, Data curation, Writing – original draft, Writing – review & editing, Visualization, Supervision, Project administration. **Daisy Rabbitt:** Validation, Formal analysis, Investigation, Data curation. **Dr Zakhar Kudrynskyi:** Validation, Formal analysis, Investigation, Data curation, Writing – original draft, Writing – review & editing, Visualization. **Dr Reda Felfel:** Validation, Writing – original draft, Writing – review & editing, Supervision. **Dr Ifty Ahmed:** Validation, Writing – original draft, Writing – review & editing, Supervision. **Prof. Adam Clare:** Validation, Writing – original draft, Writing – review & editing, Supervision, Funding acquisition. **Prof. David Grant:** Conceptualization, Methodology, Validation, Writing – original draft, Writing – review & editing, Supervision. **Prof. Liam Grover:** Writing –

review & editing, Supervision, Funding acquisition. **Dr Sophie Cox:** Conceptualization, Methodology, Validation, Resources, Writing – original draft, Writing – review & editing, Supervision, Project administration, Funding acquisition.

Declaration of Competing Interest

The authors declare that they have no known competing financial interests or personal relationships that could have appeared to influence the work reported in this paper.

Data Availability

Data will be made available on request.

Acknowledgements

This work was graciously funded through an Engineering and Physical Sciences Research Council (EPSRC) Research Grant (EP/P02341X/1), EPSRC Doctoral Prize Fellowship (grant number EP/T517902/1), EPSRC Centre for Doctoral Training in Additive Manufacturing and 3D printing (EP/L01534X/1), as well as support from an EPSRC Equipment Grant (grant code: EP/L022494/1) and UKRI Future Leaders Fellowship (MR/T017783/1). The authors would like to thank all technical help within the Wolfson building, the Centre for Additive Manufacturing, Nanoscale and Microscale Research Centre (nmRC) facilities (FEG-SEM/EDS) at the University of Nottingham, and facilities within the Healthcare Technologies Institute, School of Chemical Engineering, and School of Metallurgy and Materials at the University of Birmingham.

Appendix A. Supporting information

Supplementary data associated with this article can be found in the online version at doi:10.1016/j.jmatprotec.2023.117985.

References

Abe, T., Akamaru, S., Watanabe, K., 2004. Surface modification of Al2O3 ceramic grains using a new RF sputtering system developed for powdery materials. J. Alloy. Compd. 377, 194–201.
Abe, T., Akamaru, S., Watanabe, K., Honda, Y., 2005. Surface modification of polymer microparticles using a hexagonal-barrel sputtering system. J. Alloy. Compd. 402, 227–232.
Akande, W.O., Cao, Y., Yao, N., Soboyejo, W., 2010. Adhesion and the cold welding of gold-silver thin films. J. Appl. Phys. 107, 043519.
Ali, R., Ali, F., Zahoor, A., Shahid, R.N., He, T., Shahzad, M., Asghar, Z., Shah, A., Mahmood, A., Awais, H.B., 2021. Effect of sintering path on the microstructural and mechanical behavior of aluminum matrix composite reinforced with pre-synthesized Al/Cu core-shell particles. J. Alloy. Compd. 889, 161531.
Arblaster, J., 2015. Thermodynamic properties of silver. J. Phase Equilibria Diffus. 36, 573–591.
ASTM, 2015. Additive manufacturing: general: principles: terminology. ISO/ASTM 52900, 2015.
Behera, A., Aich, S., Theivasanthi, T., 2022. Magnetron Sputtering for Development of Nanostructured Materials, Design, Fabrication, and Characterization of Multifunctional Nanomaterials. Elsevier, pp. 177–199.
Bidulsky, R., Gobber, F.S., Bidulska, J., Ceroni, M., Kvackaj, T., Grande, M.A., 2021. Coated metal powders for laser powder bed fusion (L-PBF) processing: a review. Metals 11, 1831.
Boronin, A., Koscheev, S., Zhidomirov, G., 1998. XPS and UPS study of oxygen states on silver. J. Electron Spectrosc. Relat. Phenom. 96, 43–51.
Buhairi, M.A., Foudzi, F.M., Jamhari, F.I., Sulong, A.B., Radzuan, N.A.M., Muhamad, N., Mohamed, I.F., Azman, A.H., Harun, W.S.W., Al-Furjan, M., 2022. Review on volumetric energy density: influence on morphology and mechanical properties of Ti6Al4V manufactured via laser powder bed fusion. Prog. Addit. Manuf. 1–19.
Chawla, K.K., 2012. Metal matrix composites. Compos. Mater. 197–248 (Springer).
Chen, M., Yang, L., Zhang, L., Han, Y., Lu, Z., Qin, G., Zhang, E., 2017. Effect of nano/micro-Ag compound particles on the bio-corrosion, antibacterial properties and cell biocompatibility of Ti-Ag alloys. Mater. Sci. Eng.: C. 75, 906–917.
Clare, A.T., Reynolds, W.J., Murray, J.W., Aboulkhair, N.T., Simonelli, M., Hardy, M., Grant, D.M., Tuck, C., 2020. Laser calorimetry for assessment of melting behaviour in multi-walled carbon nanotube decorated aluminium by laser powder bed fusion. CIRP Ann. 69, 197–200.
Clayton, J., 2019. An introduction to powder characterization. Handb. Pharm. Wet. granulation 569–613 (Elsevier).
Coe, S.C., Wadge, M.D., Felfel, R.M., Ahmed, I., Walker, G.S., Scotchford, C.A., Grant, D. M., 2020. Production of high silicon-doped hydroxyapatite thin film coatings via magnetron sputtering: Deposition, characterisation, and in vitro biocompatibility. Coatings 10, 190.
Dupin, J.-C., Gonbeau, D., Vinatier, P., Levasseur, A., 2000. Systematic XPS studies of metal oxides, hydroxides and peroxides. Phys. Chem. Chem. Phys. 2, 1319–1324.
Ensinger, W., Müller, H., 1994. Surface modification and coating of powders by ion beam techniques. Mater. Sci. Eng.: A 188, 335–340.
Ensinger, W., Müller, H., 2003. Surface treatment of aluminum oxide and tungsten carbide powders by ion beam sputter deposition. Surf. Coat. Technol. 163, 281–285.
Fishman, M., Sherbaum, N., Zahavi, J., 1995. Laser cladding and alloying for refurbishing worn machine parts and improving their surface properties, 9th Meeting on Optical Engineering in Israel. SPIE, pp. 181–187.
Florando, J., 2006. Report on coating from Teer. Lawrence Livermore National Lab. (LLNL), Livermore, CA (United States).
Galindo, R.E., Benito, N., Palacio, C., Cavaleiro, A., Carvalho, S., 2013. Ag+ release inhibition from ZrCN–Ag coatings by surface agglomeration mechanism: structural characterization. J. Phys. D: Appl. Phys. 46, 325303.
Hanby, B.V., Stuart, B.W., Gimeno-Fabra, M., Moffat, J., Gerada, C., Grant, D.M., 2019. Layered Al2O3-SiO2 and Al2O3-Ta2O5 thin-film composites for high dielectric strength, deposited by pulsed direct current and radio frequency magnetron sputtering. Appl. Surf. Sci. 492, 328–336.
Hara, M., Hatano, Y., Abe, T., Watanabe, K., Naitoh, T., Ikeno, S., Honda, Y., 2003. Hydrogen absorption by Pd-coated ZrNi prepared by using Barrel-Sputtering System. J. Nucl. Mater. 320, 265–271.
Herman, H., Sampath, S., McCune, R., 2000. Thermal spray: current status and future trends. MRS Bull. 25, 17–25.
Huang, S., Narayan, R.L., Tan, J.H.K., Sing, S.L., Yeong, W.Y., 2021. Resolving the porosity-unmelted inclusion dilemma during in-situ alloying of Ti34Nb via laser powder bed fusion. Acta Mater. 204, 116522.
Johnson, P., Christy, R., 1974. Optical constants of transition metals: Ti, v, cr, mn, fe, co, ni, and pd. Phys. Rev. B 9, 5056.
Johnson, P.B., Christy, R.-W., 1972. Optical constants of the noble metals. Phys. Rev. B 6, 4370.
Kelly, P.J., Arnell, R.D., 2000. Magnetron sputtering: a review of recent developments and applications. Vacuum 56, 159–172.
Kersten, H., Schmetz, P., Kroesen, G., 1998. Surface modification of powder particles by plasma deposition of thin metallic films. Surf. Coat. Technol. 108, 507–512.
Knieps, M.S., Reynolds, W.J., Dejaune, J., Clare, A.T., Evirgen, A., 2021. In-situ alloying in powder bed fusion: The role of powder morphology. Mater. Sci. Eng.: A 807, 140849.
Kudo, E., Hibiya, S., Kawamura, M., Kiba, T., Abe, Y., Kim, K.H., Sugiyama, T., Murotani, H., 2018. Optical properties of highly stable silver thin films using different surface metal layers. Thin Solid Films 660, 730–732.
Lane, B., Zhirnov, I., Mekhontsev, S., Grantham, S., Ricker, R., Rauniyar, S., Chou, K., 2020. Transient laser energy absorption, co-axial melt pool monitoring, and relationship to melt pool morphology. Addit. Manuf. 36, 101504.
Lassègue, P., Salvan, C., De Vito, E., Soulas, R., Herbin, M., Hemberg, A., Godfroid, T., Baffie, T., Roux, G., 2021. Laser powder bed fusion (L-PBF) of Cu and CuCrZr parts: Influence of an absorptive physical vapor deposition (PVD) coating on the printing process. Addit. Manuf. 39, 101888.
Lei, Z., Zhang, H., Zhang, E., You, J., Ma, X., Bai, X., 2018. Antibacterial activities and biocompatibilities of Ti-Ag alloys prepared by spark plasma sintering and acid etching. Mater. Sci. Eng.: C 92, 121–131.
Li, J., Deng, N., Wu, P., Zhou, Z., 2019. Elaborating the Cu-network structured of the W–Cu composites by sintering intermittently electroplated core-shell powders. J. Alloy. Compd. 770, 405–410.
Lowther, M., Louth, S., Davey, A., Hussain, A., Ginestra, P., Carter, L., Eisenstein, N., Grover, L., Cox, S., 2019. Clinical, industrial, and research perspectives on powder bed fusion additively manufactured metal implants. Addit. Manuf. 28, 565–584.
Maharubin, S., Hu, Y., Sooriyaarachchi, D., Cong, W., Tan, G.Z., 2019. Laser engineered net shaping of antimicrobial and biocompatible titanium-silver alloys. Mater. Sci. Eng.: C 105, 110059.
Meier, C., Weissbach, R., Weinberg, J., Wall, W.A., Hart, A.J., 2019a. Critical influences of particle size and adhesion on the powder layer uniformity in metal additive manufacturing. J. Mater. Process. Technol. 266, 484–501.
Meier, C., Weissbach, R., Weinberg, J., Wall, W.A., Hart, A.J., 2019b. Modeling and characterization of cohesion in fine metal powders with a focus on additive manufacturing process simulations. Powder Technol. 343, 855–866.
Merstallinger, A., Sales, M., Semerad, E., Dunn, B., 2009. Assessment of cold welding between separable contact surfaces due to impact and fretting under vacuum. ESA Sci. Tech. Memo. 279, 57.
Mosallanejad, M.H., Niroumand, B., Aversa, A., Saboori, A., 2021. In-situ alloying in laser-based additive manufacturing processes: a critical review. J. Alloy. Compd. 872, 159567.
Mussatto, A., Groarke, R., O'Neill, A., Obeidi, M.A., Delaure, Y., Brabazon, D., 2021. Influences of powder morphology and spreading parameters on the powder bed topography uniformity in powder bed fusion metal additive manufacturing. Addit. Manuf. 38, 101807.
Ohtsuki, T., Smith, L., Tang, M., Pistorius, P., 2020. Origin of Oxides and Oxide-Related Pores in Laser Powder Bed Fusion Parts, Structural Integrity of Additive Manufactured Materials and Parts. ASTM International.
Pang, Y., Cao, Y., Chu, Y., Liu, M., Snyder, K., MacKenzie, D., Cao, C., 2020. Additive manufacturing of batteries. Adv. Funct. Mater. 30, 1906244.

Phua, A., Doblin, C., Owen, P., Davies, C.H., Delaney, G.W., 2021. The effect of recoater geometry and speed on granular convection and size segregation in powder bed fusion. Powder Technol. 394, 632–644.
Poelman, H., Eufinger, K., Depla, D., Poelman, D., De Gryse, R., Sels, B., Marin, G., 2007. Magnetron sputter deposition for catalyst synthesis. Appl. Catal. A: Gen. 325, 213–219.
Schmid, G., Eisenmenger-Sittner, C., 2013. A method for uniformly coating powdery substrates by magnetron sputtering. Surf. Coat. Technol. 236, 353–360.
Sciacca, G., Sinico, M., Cogo, G., Bigolaro, D., Pepato, A., Esposito, J., 2022. Experimental and numerical characterization of pure copper heat sinks produced by laser powder bed fusion. Mater. Des. 214, 110415.
Seltzman, A., Wukitch, S., 2021. Fracture characteristics and heat treatment of laser powder bed fusion additively manufactured GRCop-84 copper. Mater. Sci. Eng.: A 827, 141690.
Shaheen, M.Y., Thornton, A.R., Luding, S., Weinhart, T., 2021. The influence of material and process parameters on powder spreading in additive manufacturing. Powder Technol. 383, 564–583.
Shi, A., Zhu, C., Fu, S., Wang, R., Qin, G., Chen, D., Zhang, E., 2020. What controls the antibacterial activity of Ti-Ag alloy, Ag ion or Ti2Ag particles? Mater. Sci. Eng.: C 109, 110548.
Simonelli, M., Aboulkhair, N.T., Cohen, P., Murray, J.W., Clare, A.T., Tuck, C., Hague, R. J., 2018. A comparison of Ti-6Al-4V in-situ alloying in Selective Laser Melting using simply-mixed and satellited powder blend feedstocks. Mater. Charact. 143, 118–126.
Soro, N., Attar, H., Brodie, E., Veidt, M., Molotnikov, A., Dargusch, M.S., 2019. Evaluation of the mechanical compatibility of additively manufactured porous Ti–25Ta alloy for load-bearing implant applications. J. Mech. Behav. Biomed. Mater. 97, 149–158.
Speidel, A., Wadge, M.D., Gargalis, L., Cooper, T.P., Reynolds, W., Grant, D., Hague, R., Clare, A.T., Murray, J.W., 2022. The interaction of volatile metal coatings during the laser powder bed fusion of copper. J. Mater. Process. Technol. 299, 117332.
Stuart, B.W., Gimeno-Fabra, M., Segal, J., Ahmed, I., Grant, D.M., 2015. Degradation and characterization of resorbable phosphate-based glass thin-film coatings applied by radio-frequency magnetron sputtering. ACS Appl. Mater. Interfaces 7, 27362–27372.
Trapp, J., Rubenchik, A.M., Guss, G., Matthews, M.J., 2017. In situ absorptivity measurements of metallic powders during laser powder-bed fusion additive manufacturing. Appl. Mater. Today 9, 341–349.
Tyagi, R., Xiong, D., Li, J., 2011. Effect of load and sliding speed on friction and wear behavior of silver/h-BN containing Ni-base P/M composites. Wear 270, 423–430.
Wadge, M.D., Turgut, B., Murray, J.W., Stuart, B.W., Felfel, R.M., Ahmed, I., Grant, D.M., 2020. Developing highly nanoporous titanate structures via wet chemical conversion of DC magnetron sputtered titanium thin films. J. Colloid Interface Sci. 566, 271–283.
Wang, C., Tan, X., Du, Z., Chandra, S., Sun, Z., Lim, C., Tor, S., Lim, C., Wong, C., 2019. Additive manufacturing of NiTi shape memory alloys using pre-mixed powders. J. Mater. Process. Technol. 271, 152–161.
Wilthan, B., Cagran, C., Pottlacher, G., 2005. Combined DSC and pulse-heating measurements of electrical resistivity and enthalpy of tungsten, niobium, and titanium. Int. J. Thermophys. 26, 1017–1029.
Xu, X., Lin, X., Yang, M., Chen, J., Huang, W., 2009. Microstructure evolution in laser solid forming of Ti–50 wt % Ni alloy. J. Alloy. Compd. 480, 782–787.
Xu, Z., Yu, X., Shen, Z., 2007. Coating metals on micropowders by magnetron sputtering. China Part. 5, 345–350.
Ziewiec, K., Kędzierski, Z., Zielińska-Lipiec, A., Stępiński, J., Kąc, S., 2009. Formation, properties and microstructure of amorphous/crystalline composite Ag20Cu30Ti50 alloy using miscibility gap. J. Alloy. Compd. 482, 114–117.